*To be published in Optics Express:*

| | |
|---|---|
| **Title:** | On-chip optical pulse train generation through the optomechanical oscillation |
| **Authors:** | Xiangming Xu,Hailong Pi,Wangke Yu,Jize Yan |
| **Accepted:** | 21 September 21 |
| **Posted** | 22 September 21 |
| **DOI:** | https://doi.org/10.1364/OE.431955 |

# On-chip optical pulse train generation through the optomechanical oscillation

**XIANGMING XU, HAILONG PI, WANGKE YU, AND JIZE YAN***

*School of Electronics and Computer Science, University of Southampton, Southampton, SO17 1BJ, United Kingdom*
*J.Yan@soton.ac.uk

**Abstract:** This paper proposes a novel on-chip optical pulse train generator (OPTG) based on optomechanical oscillation (OMO). The OPTG consists of an optical cavity and mechanical resonator, in which OMO periodically modulates the optical cavity field and consequently generates optical pulse trains. The dimensionless method are introduced to simulate the OMO-based OPTG with reduced analysis complexity. We investigate the optomechanical coupling and the dynamic back-action processes, by which we found a dead zone that forbids the OMO, and derived the optimal laser detuning and the minimum threshold power. We analysed the OMO-based OPTG in terms of the pulse shape distortion, extinction ratio (ER) and duty-cycle (DC). Increasing input power, mechanical and optical Q-factors will increase ER, reduce DC and produce sharper and shorter optical pulses. We also discuss the design guidance of OMO-based OPTG and explore its application in distributed fibre optical sensor (DFOS).





## 1. Introduction

Optical pulse train generators (OPTG) are essential for many applications, such as optical communication [1], microwave photonics [2] and sensing system [3]. For instance, OPTG with a repetition rate lower than ~10GHz is highly desired for distributed fibre optical sensors (DFOS) [4]. Recently, integrated optical pulse generation is achieved by a few approaches, including mode-locked semiconductor lasers [5, 6], microresonator-based Kerr soliton frequency comb [7, 8] and on-chip optical modulator [9, 10]. The approach of semiconductor mode-locked laser does not need an extra laser, but requires phase-lock design and heterogeneous integration, which needs a complicated process flow and is usually not CMOS compatible. In addition, an external DC or RF source is also needed to activate the pump and tune the laser. The approach of microresonator-based Kerr soliton frequency comb inputs a narrow-band laser source into an optical microresonator with high quality factor, and uses the cascaded four-wave-mixing process to generate optical pulses. The soliton threshold power increases with decreasing repetition rate [8]—this power scaling leads to high power consumption for a repetition rate below ~10GHz. In addition, repetition rate reduction needs a larger cavity length, a higher Q-factor and precise dispersion control, resulting in a more challenging fabrication process. The approach of the on-chip optical modulator generates optical pulses by modulating input laser source with the electrical-optical or the thermal-optical effects. In addition to the complex fabrication process involving metallisation and doping, an external bulky radio frequency (RF) source is also needed, which are the bottleneck for the system-on-chip applications.

Recently, [11] proposed to use optomechanical systems to generate optical frequency sidebands. This method involves a parametric process and potentially can be utilised to generate time-domain pulse trains based on Fourier transformation. In [12], the author proposed to generate high-order frequency sidebands by exploring the discrete optomechanical attractors. However, the tuning is noncontinuous and pulse shape is distorted. Optomechanical systems explore the interaction between a mechanical resonator and an optical cavity [13, 14], in which a plethora of interesting optomechanical effects have been observed, including optical spring [15], bistability [16], normal-

mode splitting [17], optomechanical induced transparency [18], optomechanical cooling [19] and optomechanical oscillation (OMO) [20]. Impressive applications of OMO were also demonstrated, such as high-sensitivity force-sensing [21], photonic clock [22], microwave-optic conversion [23], and quantum information [24].

OMO is caused by the optomechanical dynamic back-action [25, 26]. The back-action reduces the overall effective damping rate of the mechanical resonator, which is the ratio of the damping coefficient to the effective mass of the mechanical resonator. It then starts the mechanical oscillation when the overall effective damping rate becomes negative. The mechanical oscillation simultaneously modulates the optical cavity field and forms a range of frequency sidebands to generate the optical pulse trains. Recently, OMO ranging from ~KHz to ~GHz has been demonstrated in various on-chip platforms using state-of-the-art nanofabrication process [22, 27–30]. In addition, no external RF source is required to maintain the oscillation. The OMO process thus provides a promising method to generate optical pulse trains.

This paper investigates the novel approach of realising on-chip OPTG with OMO and is organised as follow: Section 2 introduces the theoretical model based on four independent dimensionless parameters to analytically and numerically investigate the OMO process. We found that a dead-zone forbids the onset of OMO and derives the optimal detuning value and the minimum threshold power. Section 3 investigates the OMO-based OPTG performance regarding shape distortion, ER and DC. The resolved-sideband regime can be chosen for short optical pulse generation with less shape distortion. Pulses with targeted ER and DC can be designed with different laser detuning, optical and mechanical Q-factors, and input powers. Section 4 discusses the OMO-based OPTG design using various dimensionless parameters and considers its potential applications in DFOS.



## 2. Optical pulse generation

### 2.1. Theoretical model based on dimensionless parameters

We consider a theoretical model of optomechanical coupling as shown in Fig.1(a), in which the displacement of the mechanical resonator modulates the resonance frequency of the optical cavity. For a small mechanical displacement $x(t)$, the optomechanical coupling coefficient is defined as $G = -\partial\omega_{\mathrm{cav}}/\partial x$, where $\omega_{\mathrm{cav}}$ is the resonance frequency of the optical cavity. The field amplitude inside the cavity is $a(t)$, such that $|a(t)|^2$ can be normalised as the number of photons circulating within the cavity. When neglecting all the thermal fluctuations(including the photon shot noise and the intrinsic thermal noise), the following coupling equations describe the time evolution of the optical mode amplitude $a(t)$ and mechanical motion $x(t)$ [31],

$$\frac{da(t)}{dt} = i(\Delta + Gx(t))a(t) - \frac{\kappa}{2}a(t) + \sqrt{\kappa_{\mathrm{ex}}}s, \tag{1}$$

$$\frac{dx^2(t)}{dt^2} + \Gamma_m\frac{dx(t)}{dt} + \Omega_m^2 x(t) = \frac{\hbar G|a(t)|^2}{m_{\mathrm{eff}}}. \tag{2}$$

Eq.(1) describes the dynamics of the optical field [32], in which $\kappa$ is the photon cavity decay rate and $\kappa_{\mathrm{ex}}$ represents the part associated with the external coupling. The effective drive amplitude of the pump laser is $s$ and can be normalised as $s = \sqrt{P_{\mathrm{in}}/(\hbar\omega_L)}$, where $P_{\mathrm{in}}$ is the input laser power, $\omega_L$ is the laser frequency, $\hbar$ is the reduced Planck Constant). Here, we have introduced a rotating frame with the laser frequency $\omega_L$, i.e., $a^{\mathrm{real}}(t) = a^{\mathrm{here}}(t)e^{-i\omega_L t}$ , and laser detuning $\Delta = \omega_L - \omega_{\mathrm{cav}}$. The term $Gx(t)$ represents the optical resonance frequency shift induced by the mechanical motion. Eq.(2) describes the temporal motion of a mechanical resonator with effective mass $m_{\mathrm{eff}}$, resonance frequency $\Omega_m$ and energy damping rate $\Gamma_m$. The term on the right side of Eq.(2) is the radiation pressure force acting on the mechanical resonator. Eq.(1) and Eq.(2) can theoretically describe the physical process of optomechanical coupling and have

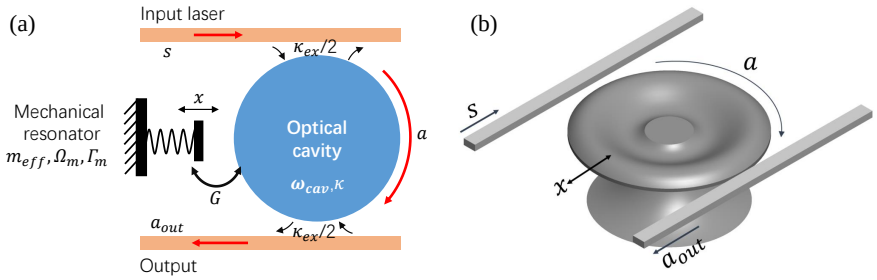


Fig. 1. (a) Schematic diagram of an optomechanical system in the WGM form with cavity resonant frequency $\omega_{\rm cav}$ and damping rate $\kappa$. The mechanical resonator with resonant frequency $\Omega_m$, damping rate $\Gamma_m$, and effective mass $m_{\rm eff}$ is coupled with the optical cavity through a coupling coefficient $G$. The optomechanical system is excited with an input light through a coupling rate $\kappa_{\rm ex}/2$, and the transmitted optical field through the drop port is the output. (b) An on-chip WGM optomechanical system composed of a microdisk resonator and two bus waveguide.

proved many optomechanical experiments with high precision, both in the linearised regime and nonlinear regime [33, 34].

In this work, we discuss an optomechanical system whose optical output field only depends on the intracavity field, for instance, the transmitted field of the drop port in an add-drop whispering gallery mode (WGM) optical cavity composed of a microdisk resonator and two bus waveguides as shown in Fig.1(b). According to the input-output relation [32], the output field can then be written as a linear relation $a_{\rm out} = \sqrt{\kappa_{\rm ex}/2}a$. Therefore, the optical output field is proportional to the intracavity field, and we use the intracavity field to calculate the optical pulse train generation in the later sessions.

For generality, it is desirable to non-dimensionalise the above coupled equations (Eq.(1) and Eq.(2)) [34, 35]. Here, we rescale the variables $t$, $a$, $x$ as $\tilde{t} = \Omega_m t$, $\tilde{a} = a\Omega_m/(2s\sqrt{k_{\rm ex}})$, $\tilde{x} = Gx/\Omega_m$, and introduce a new set of dimensionless parameters $\widetilde{\Delta} = \Delta/\Omega_m$, $\tilde{\kappa} = \kappa/\Omega_m$, $\widetilde{\Gamma_m} = \Gamma_m/\Omega_m$, $\widetilde{\kappa_{\rm ex}} = \kappa_{\rm ex}/\Omega_m$. For simplicity, we assume $\widetilde{\kappa_{\rm ex}}/\tilde{\kappa} = 0.5$, which refers to the "critical coupling" situation, and in the experiment we can vary this ratio by changing the coupling rate of the optical resonator to input/output waveguide. It deserves noting that $\widetilde{\Gamma_m} = \Gamma_m/\Omega_m$ is a direct inverse of the mechanical quality factor $Q_m$. The original coupled equations can thus be reduced to the Eq.(3) and Eq.(4) shown below:

$$\frac{d\tilde{a}}{d\tilde{t}} = i(\widetilde{\Delta} + \tilde{x})\tilde{a} - \frac{\tilde{\kappa}}{2}\tilde{a} + \frac{1}{2}, \tag{3}$$

$$\frac{d^2\tilde{x}}{d\tilde{t}^2} + \widetilde{\Gamma_m}\frac{d\tilde{x}}{d\tilde{t}} + \tilde{x} = \frac{\tilde{\kappa}\tilde{P}|\tilde{a}|^2}{2}, \tag{4}$$

Where $\tilde{P}$ is the normalised input laser power and is given by,

$$\tilde{P} = \frac{4\hbar G^2|s|^2}{m_{\rm eff}\Omega_m^4} = \frac{4P_{\rm in}G^2}{m_{\rm eff}\Omega_m^4\omega_L}. \tag{5}$$

In the above equations, we have included the real input power $P_{\rm in}$, optomechanical coupling coefficient $G$, mechanical effective mass $m_{\rm eff}$, mechanical frequency $\Omega_m$ and input laser frequency $\omega_L$ into the dimensionless input power $\tilde{P}$. The effects of these parameters can thus all be taken into account in the variation of $\tilde{P}$. By this means, the quantitative dynamics of this system will only depend on four dimensionless parameters: normalised input power $\tilde{P}$, normalised optical

cavity decay rate $\tilde{\kappa}$, normalised laser detuning $\widetilde{\Delta}$, normalised mechanical damping rate $\widetilde{\Gamma_m}$, which greatly eases the complexity of the following analysis.

### 2.2. Dynamic back-action and OMO threshold

It is well known that the above optomechanical coupling would lead to dynamic back-action due to the retarded nature of the radiation pressure force [25, 36]. We can first linearise the above inherently nonlinear equations Eq.(1) and Eq.(2) around a steady-state solution and keep only the linear terms, and then solve them in the frequency domain analytically [31]. The resulting optomechanical damping rate is then non-dimensionalised and given by,

$$\widetilde{\Gamma_{\mathrm{opt}}} = \frac{\Gamma_{\mathrm{opt}}}{\Omega_m} = \frac{\tilde{\kappa}\tilde{P}|\tilde{\bar{a}}|^2}{4}\left\{\frac{\tilde{\kappa}}{\frac{\tilde{\kappa}^2}{4}+(1+\widetilde{\bar{\Delta}})^2} - \frac{\tilde{\kappa}}{\frac{\tilde{\kappa}^2}{4}+(1-\widetilde{\bar{\Delta}})^2}\right\}, \tag{6}$$

where $\tilde{\bar{a}}$ is the averaged field amplitude in the cavity, and $\widetilde{\bar{\Delta}} = \widetilde{\Delta} + \tilde{\bar{x}}$ is the modified laser detuning caused by the averaged mechanical displacement offset $\tilde{\bar{x}}$ due to the constant optical radiation force on the mechanical resonator. They can be obtained by first linearising the coupled equations Eq.(1) and Eq.(2) and solving the resulting steady state equations,

$$\tilde{\bar{x}} = \frac{\tilde{\kappa}\tilde{P}|\tilde{\bar{a}}|^2}{2} = \frac{\tilde{\kappa}\tilde{P}}{2}\left|\frac{1}{\tilde{k}-2i(\widetilde{\Delta}+\tilde{\bar{x}})}\right|^2 = \frac{\tilde{\kappa}\tilde{P}}{8(\widetilde{\Delta}+\tilde{\bar{x}})^2+2\tilde{k}^2}. \tag{7}$$

We then use the above Eq.(7) to eliminate the parameter $\tilde{\bar{x}}$ in Eq.(6), thus the dimensionless optomechanical damping rate $\widetilde{\Gamma_{\mathrm{opt}}}$ can be obtained as a function of only three parameters: $\tilde{P}$, $\tilde{\kappa}$ and $\widetilde{\Delta}$. It can also be seen from Eq.(6) that an effectively red-detuned laser($\widetilde{\bar{\Delta}} < 0$) results in positive $\widetilde{\Gamma_{\mathrm{opt}}}$ and extra damping, while an effectively blue-detuned laser($\widetilde{\bar{\Delta}} > 0$) leads to negative $\widetilde{\Gamma_{\mathrm{opt}}}$ and anti-damping. The extra-damping on the mechanical resonator leads to optomechanical cooling [19, 26] where the mechanical vibration is suppressed, while anti-damping leads to optomechanical heating where the mechanical vibration is amplified. Eventually, the OMO emerges when the overall damping rate $\widetilde{\Gamma_{\mathrm{opt}}} + \widetilde{\Gamma_m}$ is reduced to be negative. In order to find the OMO threshold, as shown in Fig.2, we plotted the optomechanical damping rate $\widetilde{\Gamma_{\mathrm{opt}}}$ as a function of $\tilde{P}$ and $\widetilde{\Delta}$ under four different values of $\tilde{\kappa}$, namely $\tilde{\kappa} = 0.1$, $\tilde{\kappa} = 0.5$, $\tilde{\kappa} = 2$ and $\tilde{\kappa} = 10$. In each of the figures, contours for $\widetilde{\Gamma_{\mathrm{opt}}} = -0.001, -0.01, -0.1, -1$ are shown, which depict the threshold for OMO when $\widetilde{\Gamma_m} = 0.001, 0.01, 0.1, 1$.

It is clear that $\widetilde{\Gamma_{\mathrm{opt}}}$ has its maximum and minimum value for each $\tilde{\kappa}$. Therefore, there exists a maximum cooling or heating rate for a given value of $\tilde{\kappa}$, even though the input power $\tilde{P}$ varies monotonically. This can be explained by looking at Eq.(6) and Eq.(7). Input power $\tilde{P}$ and effective laser detuning $\widetilde{\bar{\Delta}}$ both contribute to the optomechanical damping rate $\widetilde{\Gamma_{\mathrm{opt}}}$ through the dynamic back-action (Eq.(6)). In the meantime, $\tilde{P}$ changes the static displacement $\tilde{\bar{x}}$ of the mechanical resonator, i.e. the effective laser detuning $\widetilde{\bar{\Delta}}$, through the optical radiation-pressure force (Eq.(7)). Therefore, the value of $\widetilde{\Gamma_{\mathrm{opt}}}$ would not be monotonically modified when monotonically varying $\tilde{P}$. The existence of a minimum value of $\widetilde{\Gamma_{\mathrm{opt}}}$ could lead to a situation where the overall damping rate $\widetilde{\Gamma_{\mathrm{opt}}} + \widetilde{\Gamma_m}$ is always positive when $\widetilde{\Gamma_m}$ is large enough. We named this situation "dead-zone effect", where no OMO can be excited under any detuning $\widetilde{\Delta}$ and $\tilde{P}$ for certain given values of $\tilde{\kappa}$ and $\widetilde{\Gamma_m}$. In the “dead zone”, the mechanical resonator still can be heated and the thermal Brownian motion is amplified. However, due to the large intrinsic mechanical damping, these optomechanical heating simply is not large enough to reduce the effective damping rate to zero, thus the optomechanical oscillation can not happen. This can be observed from Fig.2, in which we found the threshold contours for all the four different $\widetilde{\Gamma_m}$ when $\tilde{\kappa} = 0.1$, $\tilde{\kappa} = 0.5$ and $\tilde{\kappa} = 2$.

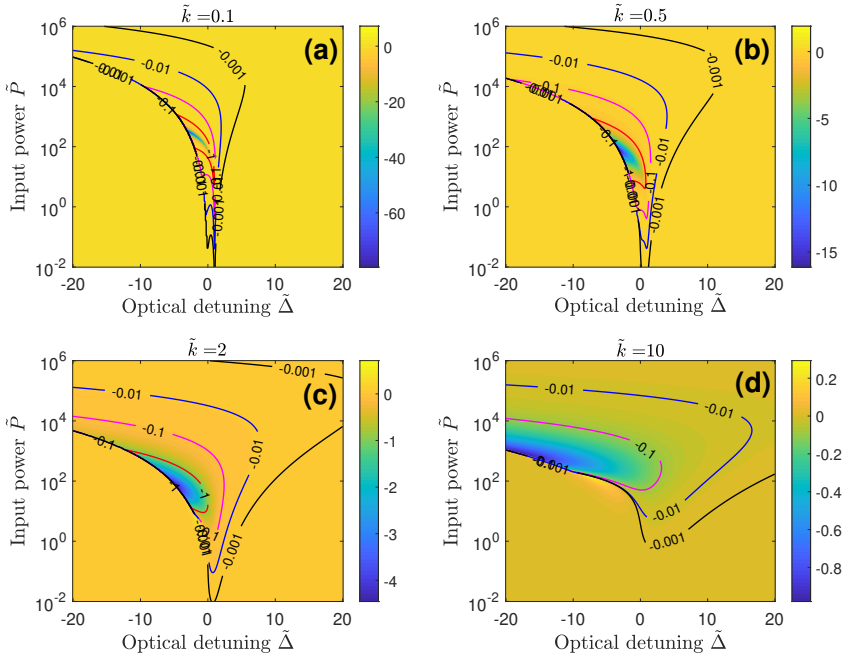


Fig. 2. (a-d) The optomechanical damping rate $\widetilde{\Gamma_{\rm opt}}$ as a function of $\tilde{P}$ and $\widetilde{\Delta}$ for $\tilde{\kappa} = 0.1$, $\tilde{\kappa} = 0.5$, $\tilde{\kappa} = 2$ and $\tilde{\kappa} = 10$, respectively. The contours in the figure show the parametric oscillation threshold for $\widetilde{\Gamma_m} = 0.001, 0.01, 0.1, 1$.



However, we found no oscillation at all for $\tilde{\kappa} = 10$ and $\widetilde{\Gamma_m} = 1$. The absence of the threshold contour for $\tilde{\kappa} = 10$ and $\widetilde{\Gamma_m} = 1$ suggests that this set of parameters lies in the dead-zone for OMO. We conducted an analysis for a wide range of $\tilde{\kappa}$ and $\widetilde{\Gamma_m}$ and the resulting dead zone is plotted in Fig.3. As shown in the figure, the dead zone appears at a combination region of low optical Q-factor and low mechanical Q-factor. When designing an OMO-based OPTG, dead zones should be avoided.

Apart from the dead-zone effect, we can also found from Fig.2 that there exists a minimum threshold power $\tilde{P}^{\rm min}_{\rm thres}$ and a corresponding optimal laser detuning $\widetilde{\Delta}_{\rm opt}$ for each $\tilde{\kappa}$ and $\widetilde{\Gamma_m}$. We here consider the situation far away from the dead-zone, which is usually the preferred case in the experiment. As shown in Fig.4(a), the OMO threshold power $\tilde{P}_{\rm thres}$ as a function of $\widetilde{\Delta}$ and $\tilde{\kappa}$ when $\widetilde{\Gamma_m} = 1/5000$ is plotted as a surface. In the valley of the curve, the minimum threshold power is marked as a black line. The projection of this line to the side and bottom can be viewed as the minimum threshold power $\tilde{P}^{\rm min}_{\rm thres}$ and corresponding optimal laser detuning $\widetilde{\Delta}_{\rm opt}$. In Fig.4(b), we have introduced a normalised optimal detuning factor defined as $\widetilde{\Delta}^{\rm norm}_{\rm opt} = \widetilde{\Delta}_{\rm opt}/(1+\tilde{\kappa})$, which is plotted as a function of $\tilde{\kappa}$ with a blue line. It can be found that in the resolved sideband regime ($\tilde{\kappa} \ll 1$), the laser detuning associated with the minimum threshold power is approaching $\widetilde{\Delta} = 1$, while in the unresolved sideband regime($\tilde{\kappa} \gg 1$), the optical laser detuning is around $0.2\tilde{\kappa}$. This suggests an optimal detuning $\Delta_{\rm opt} = \Omega_m$ in the resolved-sideband regime, and $\Delta_{\rm opt} = 0.2\kappa$ in the unresolved-sideband regime. The associated minimum power $\tilde{P}^{\rm min}_{\rm thres}$ is also plotted along with $\tilde{\kappa}$. The minimum threshold power increases with $\tilde{\kappa}$ in unresolved sideband regime, while keeping as a constant in the resolved sideband regime. It shows that an optomechanical system in the resolved sideband regime requires less optical input power to start OMO. This is because smaller $\tilde{\kappa}$ means higher optical Q-factor, which enhances the cavity field and leads to a larger

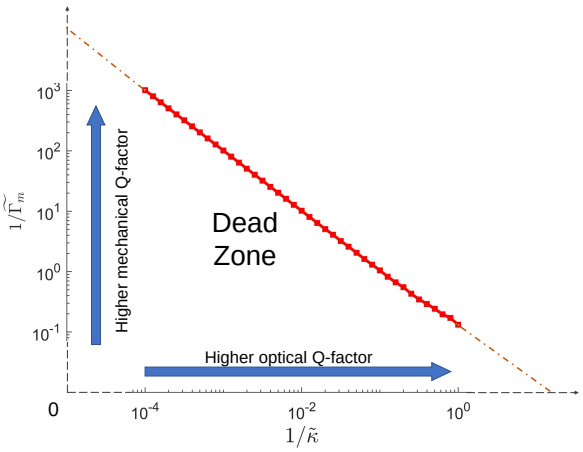


Fig. 3. OMO dead-zone shown as a relationship of $\widetilde{\Gamma_m}$ and $\tilde{\kappa}$. In the dead-zone, no oscillation will occur under any $\tilde{\Delta}$ and $\tilde{P}$

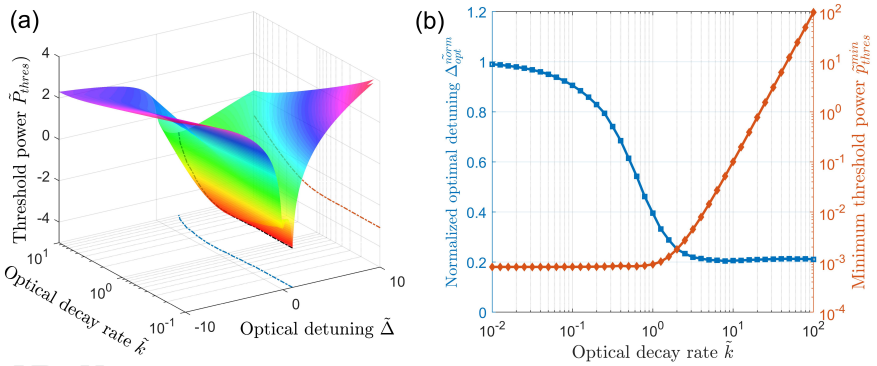


Fig. 4. (a) Threshold power $\tilde{P}_{\text{thres}}$ as a function of $\tilde{\kappa}$ and $\widetilde{\Delta}$ when $\widetilde{\Gamma_m} = 1/5000$. (b)The minimum threshold power $\tilde{P}_{\text{thres}}^{\text{min}}$ and corresponding normalised optimal detuning $\widetilde{\Delta}_{\text{opt}}^{\text{norm}} = \widetilde{\Delta}_{opt}/(1+\tilde{\kappa})$ as function of $\tilde{\kappa}$

field amplitude. A larger field amplitude would then lead to a larger optomechanical heating rate as derived in Eq.(6) and make the OMO easier to start.

As a summary, here, we analysed the optomechanical dynamic back-action effect and the OMO threshold. A dead-zone is found with a combination of low optical Q-factor and mechanical Q-factor. Minimum optical threshold power and the corresponding optimal laser detuning are derived.

### *2.3. Frequency sideband formation and optical pulse generation*

When the overall damping rate $\widetilde{\Gamma_{\text{eff}}} = \widetilde{\Gamma_{\text{opt}}} + \widetilde{\Gamma_m}$ becomes negative, the mechanical resonator starts to oscillate when small initial fluctuations occur, for instance, originated from the Brownian thermal noise induced random vibrations. Due to the nonlinear saturation effect which balances the gain and loss of the mechanical resonator, a steady-state regime is reached and the mechanical resonator oscillates at a fixed amplitude.

An ansatz can be made that the mechanical resonator is oscillating with an approximately sinusoidal pattern as $\tilde{x}(\tilde{t}) = \bar{\tilde{x}} + \tilde{A}\cos(\tilde{t})$, where $\bar{\tilde{x}}$ is the averaged displacement and $\tilde{A}$ is the

oscillation amplitude. The intracavity field can then be analytically derived through solving the differential equation Eq.(3), and we can get [37],

$$\tilde{a}(\tilde{t}) = \sum_{n=-\infty}^{\infty} \frac{J_n(-\tilde{A})}{\tilde{\kappa} - 2i(\tilde{\Delta} + \tilde{\bar{x}} - n)} e^{in\tilde{t} + i\tilde{A}\sin(\tilde{t})}. \tag{8}$$

Here, $J_n$ is the Bessel function of the first kind, so that the photon number inside the cavity is given by,

$$|\tilde{a}(\tilde{t})|^2 = \sum_{n,m=-\infty}^{\infty} \frac{J_n(-\tilde{A})J_m(-\tilde{A})e^{i(n-m)\tilde{t}}}{\left\{\tilde{\kappa} - 2i(\tilde{\Delta} + \tilde{\bar{x}} - n)\right\}\left\{\tilde{\kappa} + 2i(\tilde{\Delta} + \tilde{\bar{x}} - n)\right\}}. \tag{9}$$

The resulting cavity field consists of a range of frequency sidebands at mechanical harmonics $\pm n\Omega_m$, where $n$ is an integer. These frequency sidebands can lead to time-domain optical pulses generation according to Fourier transformation theory.

In summary, the optomechanical dynamic back-action can lead to the generation of OMO when the dead-zone is avoided, and the threshold condition is exceeded. The OMO process can then generate multiple frequency sidebands in the optical cavity and form the optical pulse trains in the time domain. In the next section, we will evaluate the performance of the OMO-based OPTG and provide design guidance.

## 3. Optical pulse characteristics and parameter analysis

The coupled differential equations Eq.(3) and Eq.(4) can be solved using the explicit Runge-Kutta method based on Dormand-Prince pair [38] to characterise the OMO based optical pulse characteristics with system parameters variations.



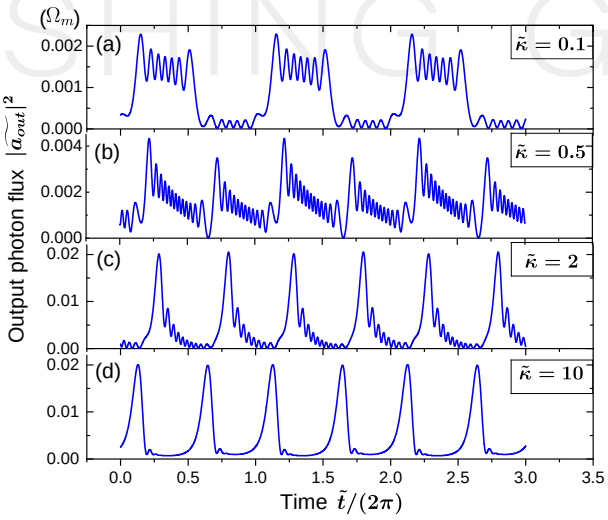


Fig. 5. (a-d) Optical pulse generation with normalised optical cavity decay rates $\tilde{\kappa} = 0.1, 0.5, 2, 10$, respectively. Other parameters are kept as constant: $\widetilde{\Gamma_m} = 1/1000$, $\tilde{\Delta} = 1$, $\tilde{P} = 100$.

As shown in Fig.5, we plotted the normalised output optical photon flux $|\widetilde{a_{\text{out}}}|^2 = \kappa_{\text{ex}}|\widetilde{a}|^2/2$ with time under different $\tilde{\kappa}$ and constant value of $\widetilde{\Gamma_m} = 1/1000$, $\tilde{\Delta} = 1$, $\tilde{P} = 100$, in which two optical pulses are generated during one mechanical oscillation period, and the mechanical frequency $\Omega_m$ determines the repetition rate of the optical pulse. On the other hand, $\Omega_m$ significantly affects the normalised input laser power $\tilde{P}$ as derived in Eq.(5), which means an optomechanical system

with a large mechanical frequency $\Omega_m$ requires higher real power $P_{in}$ to obtain the optical pulse with the same ER and DC.

In the resolved-sideband regime ($\tilde{\kappa} \ll 1$), the generated optical pulse has many ripples, which is not desired for practical applications. With the increase of $\tilde{\kappa}$, the ripples gradually disappear, and short and smooth optical pulses can be obtained with the repetition rate at $2\Omega_m$ in the unresolved-sideband regime ($\tilde{\kappa} \gg 1$).

This can be explained from two aspects. On the one hand, in the unresolved-sideband regime, the optomechanical oscillation amplitude can be substantial. The corresponding cavity detuning between input laser wavelength and optical cavity resonance wavelength oscillates between large negative and positive values [33, 39]. On the other hand, the optical cavity can respond instantaneously to the fast mechanical oscillation in the unresolved-sideband regime due to the low cavity decay rate. Therefore, during an oscillation period, the cavity field is very low most of the time due to large detuning. When the cavity detuning oscillates back to the resonant condition, the cavity field rapidly builds up and kicks the resonator out of resonance. By this means, the sharp optical pulse is generated, and OMO continues. Therefore, we will focus on the optical pulse analysis in the unresolved-sideband regime ($\tilde{\kappa} \gg 1$).

To evaluate the OMO-based OPTG and provide guidance for OMO-based OPTG design, we plot the simulated mechanical oscillation amplitude $\tilde{A}$, the ER and DC of the generated optical pulse under different system parameter in Fig.6. Normalised input power $\tilde{P}$ with value from $10^{-1}$ to $10^{4}$, normalised mechanical damping rate $\widetilde{\Gamma_m}$ from $10^{-6}$ to $10^{-2}$ are simulated for optomechanical system with $\tilde{\kappa} = 10, 40, 100$ respectively. The laser detuning $\widetilde{\Delta}$ is set to an optimised value associated with a minimum threshold power(see Section 2.2). Fig.6 thus shows explicitly the characteristics of the generated optical pulse. Larger ER and smaller DC represent a sharper and shorter optical pulse.

It is clear that both the $\tilde{A}$ and ER increase linearly with input power $\tilde{P}$, while the DC decreases with $\tilde{P}$. This means a higher input power is needed to produce a sharper and shorter optical pulse. As shown in the figures for oscillation amplitude $\tilde{A}$ and ER of the generated pulse, the direct correlation between $\tilde{A}$ and ER can be understood that larger oscillation amplitude leads to deeper modulation of the optical field and thus a sharper optical pulse. When comparing the parallel lines with different colours representing different $\widetilde{\Gamma_m}$, it is clear that smaller $\widetilde{\Gamma_m}$ (larger mechanical Q-factor $Q_m$) leads to larger $\tilde{A}$, ER, and smaller DC. Quantitatively, $\tilde{A}$ and ER both increase by 3dB when $\widetilde{\Gamma_m}$ decreases by one order of magnitude. The discrepancies for large $\tilde{P}$ are caused by the insufficient simulation time due to the limited computational resources when solving the differential equations. From the figures with varying $\tilde{\kappa}$, even though larger $\tilde{\kappa}$ leads to better pulse shape with suppressed ripples, it decreases $\tilde{A}$ and ER when other parameters remain the same. This is because larger $\tilde{\kappa}$ represents lower optical Q-factor, lower cavity enhancement and weaker field amplitude, which will decrease the OMO amplitude and ER.

Regarding the laser detuning $\widetilde{\Delta}$, we know from Section 2.2 that there exists an optimal value of $\widetilde{\Delta}$ for each $\tilde{\kappa}$ in terms of minimising the threshold power for OMO. This optimal value for threshold is not necessarily the same as the optimal value for OMO-based OPTG. To illustrate the role of $\widetilde{\Delta}$, we derived the amplitude-dependent effective optomechanical damping rate $\widetilde{\Gamma_{\text{opt}}}(\tilde{A})$, which was introduced in [35] to analyse the optomechanical multistability effect. It is defined as:

$$\widetilde{\Gamma_{\text{opt}}}(\tilde{A}) = \frac{\Gamma_{\text{opt}}(\tilde{A})}{\Omega_m} = \frac{- < F\dot{x} >}{m_{\text{eff}}\Omega_m < \dot{x}^2 >}, \tag{10}$$

Where $F$ is the radiation pressure force acting on the mechanical oscillator. For low amplitude with $\tilde{A} \to 0$, Eq.(10) can be simplified to Eq.(6). In the steady-state, the time-averaged power into the mechanical oscillator by optical force $F$ has to equal the loss due to damping $\Gamma_m$, which is $\widetilde{\Gamma_{\text{opt}}} = -\widetilde{\Gamma_m}$.

Fig.7 plotted the $\widetilde{\Gamma_{\text{opt}}}$ as a function of $\widetilde{\Delta}$ and $\tilde{A}$ when $\tilde{\kappa} = 10$ and $\tilde{P} = 1$. The contour lines

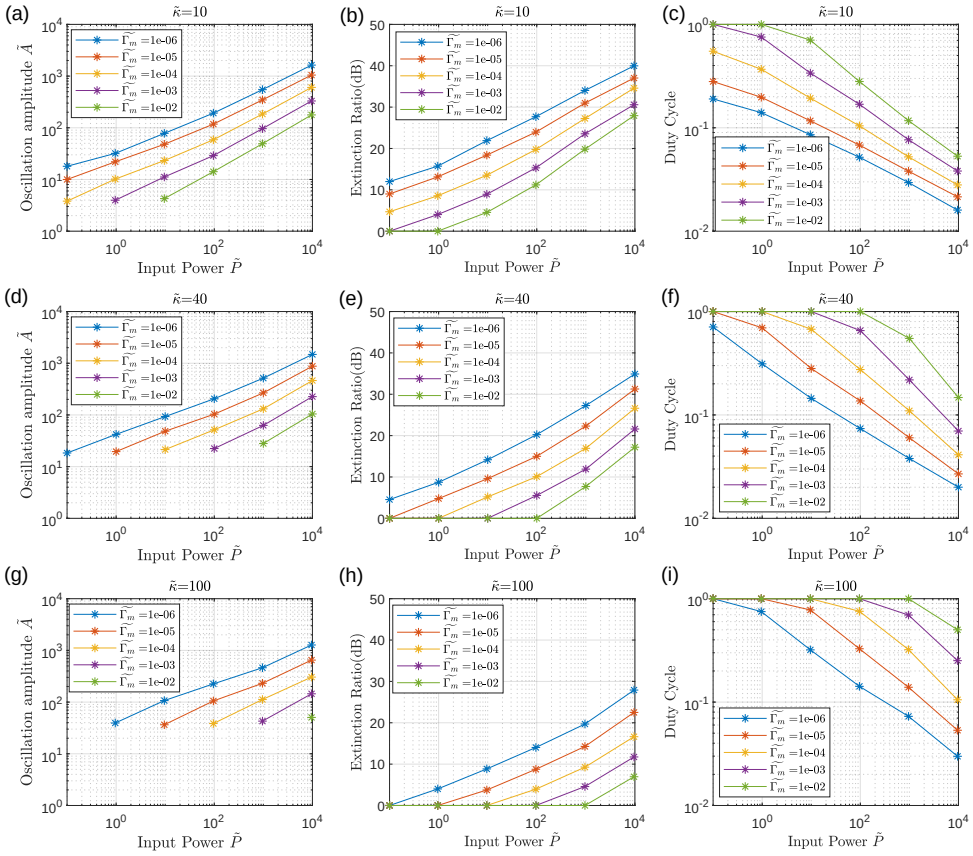


Fig. 6. The characteristics of the generated optical pulse under different parameters. (a,d,g) The mechanical oscillation amplitude $\tilde{A}$ variation with $\tilde{P}$ and $\widetilde{\Gamma_m}$ when $\tilde{\kappa} = 10$, $\tilde{\kappa} = 40$, $\tilde{\kappa} = 100$, respectively. (b,e,h) The ER variation with $\tilde{P}$ and $\widetilde{\Gamma_m}$ when $\tilde{\kappa} = 10$, $\tilde{\kappa} = 40$, $\tilde{\kappa} = 100$, respectively. (c,f,i) The DC variation with $\tilde{P}$ and $\widetilde{\Gamma_m}$ when $\tilde{\kappa} = 10$, $\tilde{\kappa} = 40$, $\tilde{\kappa} = 100$, respectively. The laser detuning $\tilde{\Delta}$ is set to a constant at the optimal value associated with a minimum threshold power.

$\widetilde{\Gamma_{\text{opt}}} = -1e-4$ indicates the possible steady state when $\widetilde{\Gamma_m} = 1e-4$. Note that stable solutions are given by the upper part of the contour line where $\widetilde{\Gamma_{\text{opt}}}$ increases with increasing $\tilde{A}$ (the upper solid continuous half of the line). The maximum heating rate when $\tilde{A} \to 0$ appears around $\widetilde{\Delta} = 2$, which agrees with the numerical simulation results in Section 2.2.

The steady-state mechanical oscillation amplitude $\tilde{A}$ increases with $\widetilde{\Delta}$, so as the ER from the above analysis for Fig.6. For the small value of $\widetilde{\Delta}$ (0 to 10 in Fig.7), we can see the onset of OMO starts from $A = 0$, which is an example of a Hopf bifurcation. However, for a larger value of $\widetilde{\Delta}$, the mechanical resonator cannot oscillate from $\tilde{A} = 0$, but have to start from a nonzero initial value. This is similar to what has been experimentally demonstrated in mechanical parametric vibration energy harvesters [40, 41]. Based on the feature, we can gradually adjust the $\widetilde{\Delta}$ to increase the oscillation amplitude and generate a shorter and sharper optical pulse to the extent that can not be acquired from zero initial condition.

Here, we have analysed OMO-based OPTG characteristics and evaluated its performance in shape distortion, ER and DC under different system parameters. Pulses with various ER and DC can be designed with different laser detuning, optical and mechanical Q-factors, and input power.

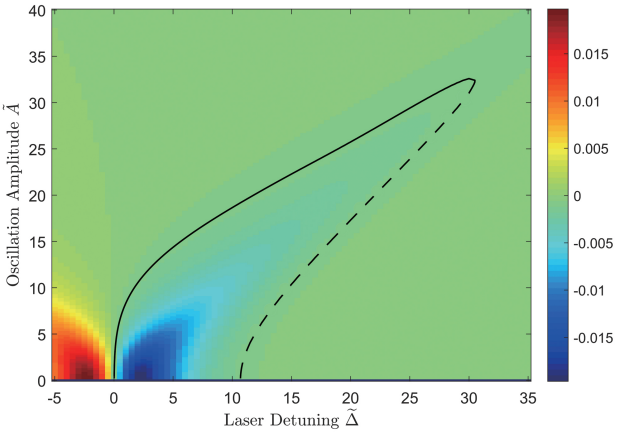


Fig. 7. The amplitude-dependent effective optomechanical damping rate $\widetilde{\Gamma_{\text{opt}}}$ as a function of $\widetilde{\Delta}$ and $\tilde{A}$ when $\tilde{\kappa} = 10$ and $\tilde{P} = 1$. The contour line shows the possible steady-state when $\widetilde{\Gamma_m} = 1e - 4$.



## 4. Optomechanical pulse generation for DFOS application

### 4.1. Optomechanical system design

In the above sessions, we used four dimensionless parameters to analyse the OMO-based OPTG with different system parameters in terms of power threshold, ER, DC and pulse shape. In reality, the optomechanical system needs to be sophisticatedly designed to obtain the desired optical pulse that suits the practical application requirements. During the design of an OMO-based OPTG, we can decouple and independently design the optical and mechanical resonator. In this way, which significantly improve design flexibility and efficiency.

A large number of previously demonstrated devices can work as roadmaps when designing an application-oriented optomechanical system. Mechanical frequency $\Omega_m$–decides the optical pulse repetition rate, with values varying from ~KHz (suspended mirror), ~MHz (suspended nanobeam, microtoroid) to ~GHz (photonic crystal cavity) have been demonstrated. Optomechanical devices with effective mss $m_{\text{eff}}$ ranging from g to zg have been realised [31], and remarkably large optomechanical coupling coefficient $G$ of around 100 GHz nm$^{-1}$ have been obtained in the photonic crystal structure [42]. It should be noted that $\Omega_m$, $m_{\text{eff}}$ and $G$ are all part of the normalised input power $\tilde{P}$ from Eq.(5). Increasing $G$ and decreasing $\Omega_m$ or $m_{\text{eff}}$ result in a larger value of $\tilde{P}$.

In addition, the Q-factor of the on-chip optical cavity can be very high in the order of millions, such as the silica microtoroid structure [43] and the $Si_3N_4$ microresonator fabricated using the Damascene process [44]. The Q-factor of micro-nano mechanical resonator also saw breakthrough these years by sophisticated elastic phononic engineering [45], and an exceptionally low mechanical dissipation and Q-factor as high as 800 million was realised [46]. Therefore, we have flexible design space for the OMO-based OPTG to suit various applications.

### 4.2. Pulse generation for DFOS

Here, we offer a design example to realise OMO-based OPTG for the DFOS application. In some DFOSs, we send a set of pulses to the fibre and measure the backscattered optical signal to sense the measurands along the fibre distributedly [4].

The criteria for DFOS can include sensing range, measurement time, measurand resolution and spatial resolution. The sensing distance is the length of the sensing fibre under test and dictates

the maximum repetition rate of the OPTG, which should be low enough to avoid overlapping the backscatter signals between the pulses from the fibre. The measurement time is the data reading and analysis time of DFOS to achieve the required measurand resolution. It sometimes needs to cover many cycles of averaging to improve the signal-to-noise ratio. It can be reduced by enhancing the ER [47, 48]. For our OMO-based OPTG, both the repetition rate and ER can be varied significantly to fit the various DFOS system requirements.

The measurand resolution and spatial resolution are the ability of the sensor to distinguish small measurand value changes and the measurand values at closely spaced locations, respectively. It has been proved that measurand resolution and spatial resolution are correlated to each other, and there is a trade-off between them [4]. A finer spatial resolution requires a narrower optical pulse, which, however, requires a wider detection bandwidth and degrades the measurand resolution. Therefore, the single optical pulse must be evaluated cooperatively in both the time(T)–domain and frequency(F)–domain. In [49], the author proposed to use the Time-Frequency (T-F) localisation to evaluate the optical pulse quality for DFOS. T-F localisation describes the extent to that a pulse signal is restricted in both the T–domain and F–domain. The mean square deviation of the time and frequency distribution of a signal is defined as,

$$\Delta T^2 = \int_{-\infty}^{+\infty} t^2 |f(t)^2|, \tag{11}$$

$$\Delta F^2 = \int_{-\infty}^{+\infty} f^2 |F(f)^2|, \tag{12}$$

Where $\Delta T$ and $\Delta F$ are the variance of the signal $f$ in T–domain and F–domain, respectively. Smaller $\Delta T$ and $\Delta F$ means the pulse performs better in time and frequency localisation. The product $\Delta T \times \Delta F$ can be used as an evaluation factor for the pulse performance evaluation.



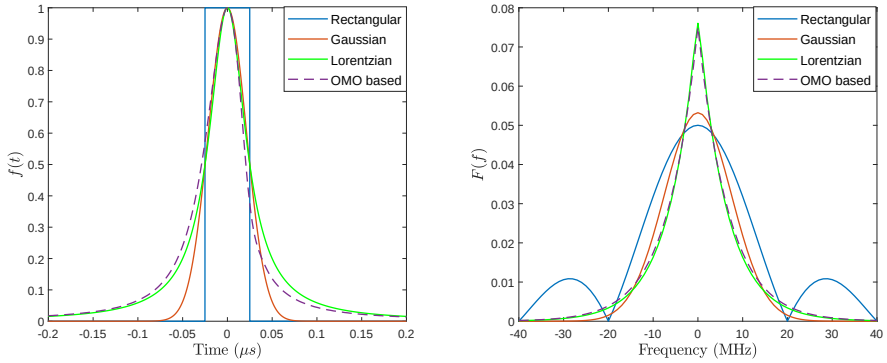


Fig. 8. Comparison between OMO based optical pulse and the traditional optical pulses (a) in time-domain. (b) in frequency-domain. The pulses all have 50 ns FWHM and 1$\mu$s period. The OMO based optical pulse is generated in an optomechanical system with $\tilde{\kappa} = 100$.

We compare the optical pulse generated in OMO-based OPTG with Rectangular, Gaussian and Lorentzian pulse shape to evaluate their T-F localisation. The pulses all have 50 ns FWHM and 1 $\mu$s period, and the OMO-based optical pulse is generated with an optomechanical system with $\tilde{\kappa}$=100. The T–domain and F–domain of the pulses were plotted in Fig.8. The T–domain and F–domain variances obtained by Eq.(11) and Eq.(12) for the four pulse shapes and their product are given in Table 1. In terms of T-F localisation, the OMO based optical pulse is close to Lorentzian and Gaussian shapes, which are much better than the widely used Rectangular

shape in DFOS. The OMO-based OPTG is also much more straightforward than the traditional pulse generator used in DFOS, which usually requires function generators, EOM or AOM.

Table 1. **Variance in the time-domain and frequency-domain with the product of the two variances for different optical pulse shapes**

| | Rectangular | Gaussian | Lorentzian | OMO based |
|---|---|---|---|---|
| $\Delta T$ | 3.23e-12 | 2.91e-12 | 4.79e-12 | 4.86e-12 |
| $\Delta F$ | 8.38e+10 | 1.03e+9 | 8.92e+8 | 9.48e+8 |
| $\Delta T \times \Delta F$ | 0.2706 | 0.003 | 0.0043 | 0.0046 |

As shown in Fig.9, we use the Brillouin Optical time domain reflectometer (BOTDR) as an example to consider a real OMO-based OPTG for DFOS applications. The function generator and EOM which are used to generate the optical pulses in traditional BOTDR can be replaced by the proposed OMO-based OPTG. The OMO-based OPTG is formed by suspending part of a racetrack-shape microresonator, where the suspended beam serves as the mechanical resonator and coupled to the optical cavity. Similar structure has been experimentally demonstrated to exhibit large amplitude optomechanical oscillation [39].

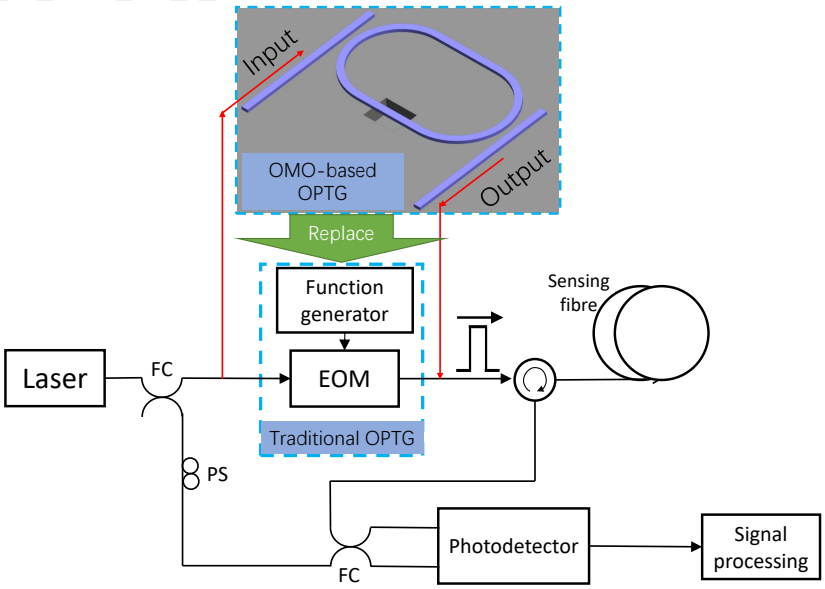


Fig. 9. The schematic of a BOTDR system, in which the optical pulse generation using function generator and EOM can be replaced by the proposed OMO-based OPTG. The OMO-based OPTG is formed by suspending part of a racetrack-shape microresonator, where the suspended beam serves as the mechanical resonator and coupled to the optical cavity. FC: Fibre coupler, PS: Polarisation scrambler.

We consider a BOTDR application with a 50$m$ fibre sensing range, a typical pulse shape with 10 ns pulse width and repetition rate of 2 MHz, which maps the DC as 0.02. We assume the device is made on a commercially available SOI wafer with 110 $nm$ thick top silicon layer. To generate a pulse with 2 MHz, we thus need a mechanical frequency at 1 MHz, which can be realised by using a suspended beam with dimensions of 30 $\mu m \times 500\ nm \times 110\ nm$ through the

Finite Element Analysis (FEA). The effective mass is calculated to be 3.8 $pg$. By under-etching the beam by 250 $nm$, we can get an optomechanical coupling coefficient $G = 1$ GHz nm$^{-1}$. We assume other system parameters are $\tilde{\kappa} = 100$, $\widetilde{\Gamma_m} = 1e-6$, which map the optical quality factor to be $1.93 \times 10^6$ and mechanical quality factor at $1 \times 10^6$. By looking at the blue line in Fig.6 (i), it is inferred that a normalised input power at around $\tilde{P} = 3e4$ is needed to generate such an optical pulse. The real input power $P_{in}$ is thus found to be 2.8 $\mu W$ according to the Eq.(5). The optomechanical system parameters to realise such a BOTDR application is summarised below,

Table 2. **Optomechanical parameters to generate OMO based optical pulse for a BOTDR application**

| | |
|---|---|
| Mechanical resonator dimension | 30 $\mu m \times 500$ $nm \times 110$ $nm$ |
| Mechanical frequency ($\Omega_m/2\pi$) | 1 MHz |
| Mechanical Q-factor ($Q_m$) | $1 \times 10^6$ |
| Optical Q-factor ($Q_O$) | $1.93 \times 10^6$ |
| Laser wavelength ($\lambda_L$) | 1550 nm |
| Effective mass ($m_{\text{eff}}$) | 3.8 pg |
| Optomechanical coupling coefficient ($G/2\pi$) | 1 GHz/nm |
| Input power ($P_{in}$) | 2.8 $\mu W$ |



Here, we demonstrated numerically that the OMO-based OPTG can fulfil the pulse generation requirement of a BOTDR [50] for short distance sensing applications, for instance, structure health monitoring and battery safety management.

## 5. Discussion and conclusion



In summary, we proposed to use the OMO process to realise an on-chip OPTG. We conducted an extensive analysis by introducing and solving a set of dimensionless equations describing the optomechanical coupling process, by which we limit the discussion to only four system parameters: normalised input power $\tilde{P}$, normalised optical cavity decay rate $\tilde{\kappa}$, normalised laser detuning $\tilde{\Delta}$ and normalised mechanical damping rate $\widetilde{\Gamma_m}$.

The dynamic back-action of the optomechanical system and the threshold of optical pulse generation is analytically and numerically investigated. We found that there exists a dead-zone for a certain value of $\tilde{\kappa}$ and $\widetilde{\Gamma_m}$, where no OMO can be observed under any $\tilde{\Delta}$ and $\tilde{P}$. Outside the dead-zone, there is an optimal laser detuning $\tilde{\Delta}_{\text{opt}}$ for each $\tilde{\kappa}$ and $\widetilde{\Gamma_m}$ where the threshold power $\tilde{P}_{\text{thres}}$ is minimum. We then study the optical pulse performance in terms of pulse shape, ER, DC for various system parameters. The shape of the pulse turns out to be ideal in the unresolved-sideband regime ($\tilde{\kappa} \gg 1$), while in the resolved-sideband($\tilde{\kappa} \ll 1$) regime, the pulse is a distorted shape with ripples. Increasing $\tilde{P}$ and decreasing $\widetilde{\Gamma_m}$ both lead to pulse generation with larger ER and smaller DC. We also derived the amplitude-dependent effective optomechanical damping rate change with $\tilde{\Delta}$, it was found $\widetilde{\Delta}$ can be gradually adjusted to generate a shorter and sharper optical pulse to an extend which is not accessible from zero initial value. Lastly, we discuss the flexible design space when we use these dimensionless parameters to design such an optical pulse generator. We consider its potential applications and benefits for the on-chip DFOS system.

Compared to the traditional integrated optical pulse generation methods using mode-locked laser which involves complicated fabrication process, this method provides simple and straightforward

fabrication process. However, we also need to note that this OMO-based OPTG needs an extra narrow-band laser, which is not required in the mode-locked laser. The full-integration of the OMO-based OPTG would require an on-chip laser source. Compared to the Kerr soliton frequency comb and on-chip modulation method, the OMO-based OPTG provides a larger variation range on repetition rate and requires no external RF source. It is intriguing that the unresolved sideband regime (low optical Q factor, $\tilde{\kappa} \gg 1$) is preferable to pursue better optical pulse shape, which greatly reduces the requirement of high-precision fabrication.

**Funding.** Engineering and Physical Sciences Research Council (EP/V000624/1); China Scholarship Council.

**Disclosures.** The authors declare no conflicts of interest.

**Data availability.** Data underlying the results presented in this paper are available from the corresponding authors upon reasonable request.

## References

1. A. Misra, C. Kress, K. Singh, S. Preußler, J. C. Scheytt, and T. Schneider, "Integrated source-free all optical sampling with a sampling rate of up to three times the rf bandwidth of silicon photonic mzm," Opt. express **27**, 29972–29984 (2019).
2. D. Marpaung, J. Yao, and J. Capmany, "Integrated microwave photonics," Nat. photonics **13**, 80–90 (2019).
3. Y. Yu, L. Luo, B. Li, K. Soga, and J. Yan, "Quadratic time-frequency transforms-based brillouin optical time-domain reflectometry," IEEE Sensors J. **17**, 6622–6626 (2017).
4. A. H. Hartog, *An introduction to distributed optical fibre sensors* (CRC Press, Taylor & Francis Group, 2017).
5. H. Wang, L. Kong, A. Forrest, D. Bajek, S. E. Haggett, X. Wang, B. Cui, J. Pan, Y. Ding, and M. A. Cataluna, "Ultrashort pulse generation by semiconductor mode-locked lasers at 760 nm," Opt. express **22**, 25940–25946 (2014).
6. E. Vissers, S. Poelman, C. O. de Beeck, K. Van Gasse, and B. Kuyken, "Hybrid integrated mode-locked laser diodes with a silicon nitride extended cavity," Opt. Express **29**, 15013–15022 (2021).
7. K. Saha, Y. Okawachi, B. Shim, J. S. Levy, R. Salem, A. R. Johnson, M. A. Foster, M. R. Lamont, M. Lipson, and A. L. Gaeta, "Modelocking and femtosecond pulse generation in chip-based frequency combs," Opt. express **21**, 1335–1343 (2013).
8. J. Liu, E. Lucas, A. S. Raja, J. He, J. Riemensberger, R. N. Wang, M. Karpov, H. Guo, R. Bouchand, and T. J. Kippenberg, "Photonic microwave generation in the x-and k-band using integrated soliton microcombs," Nat. Photonics **14**, 486–491 (2020).
9. M. Zhang, B. Buscaino, C. Wang, A. Shams-Ansari, C. Reimer, R. Zhu, J. M. Kahn, and M. Lončar, "Broadband electro-optic frequency comb generation in a lithium niobate microring resonator," Nature **568**, 373–377 (2019).
10. S. Liu, K. Wu, L. Zhou, L. Lu, B. Zhang, G. Zhou, and J. Chen, "Optical frequency comb and nyquist pulse generation with integrated silicon modulators," IEEE J. Sel. Top. Quantum Electron. **26**, 1–8 (2019).
11. M.-A. Miri, G. D'Aguanno, and A. Alù, "Optomechanical frequency combs," New J. Phys. **20**, 043013 (2018).
12. P. Djorwe, J. Effa, and S. N. Engo, "Multistability, staircases, and optical high-order sideband combs in optomechanics," JOSA B **37**, A36–A44 (2020).
13. T. J. Kippenberg and K. J. Vahala, "Cavity optomechanics: back-action at the mesoscale," Science **321**, 1172–1176 (2008).
14. M. Aspelmeyer, P. Meystre, and K. Schwab, "Quantum optomechanics," Phys. Today **65**, 29–35 (2012).
15. B. S. Sheard, M. B. Gray, C. M. Mow-Lowry, D. E. McClelland, and S. E. Whitcomb, "Observation and characterization of an optical spring," Phys. Rev. A **69**, 051801 (2004).
16. A. Dorsel, J. D. McCullen, P. Meystre, E. Vignes, and H. Walther, "Optical bistability and mirror confinement induced by radiation pressure," Phys. Rev. Lett. **51**, 1550 (1983).
17. S. Gröblacher, K. Hammerer, M. R. Vanner, and M. Aspelmeyer, "Observation of strong coupling between a micromechanical resonator and an optical cavity field," Nature **460**, 724–727 (2009).
18. S. Weis, R. Rivière, S. Deléglise, E. Gavartin, O. Arcizet, A. Schliesser, and T. J. Kippenberg, "Optomechanically induced transparency," Science **330**, 1520–1523 (2010).
19. A. Schliesser, O. Arcizet, R. Rivière, G. Anetsberger, and T. J. Kippenberg, "Resolved-sideband cooling and position measurement of a micromechanical oscillator close to the heisenberg uncertainty limit," Nat. Phys. **5**, 509–514 (2009).
20. H. Rokhsari, T. J. Kippenberg, T. Carmon, and K. J. Vahala, "Radiation-pressure-driven micro-mechanical oscillator," Opt. Express **13**, 5293–5301 (2005).
21. B. Guha, P. E. Allain, A. Lemaître, G. Leo, and I. Favero, "Force Sensing with an Optomechanical Self-Oscillator," Phys. Rev. Appl. **14**, 024079 (2020).
22. X. Luan, Y. Huang, Y. Li, J. F. McMillan, J. Zheng, S.-W. Huang, P.-C. Hsieh, T. Gu, D. Wang, A. Hati, D. A. Howe, G. Wen, M. Yu, G. Lo, D.-L. Kwong, and C. W. Wong, "An integrated low phase noise radiation-pressure-driven optomechanical oscillator chipset," Sci. reports **4**, 1–7 (2014).

23. R. W. Andrews, R. W. Peterson, T. P. Purdy, K. Cicak, R. W. Simmonds, C. A. Regal, and K. W. Lehnert, "Bidirectional and efficient conversion between microwave and optical light," Nat. Phys. **10**, 321–326 (2014).
24. A. Reed, K. Mayer, J. Teufel, L. Burkhart, W. Pfaff, M. Reagor, L. Sletten, X. Ma, R. Schoelkopf, E. Knill, and K. Lehnert, "Faithful conversion of propagating quantum information to mechanical motion," Nat. Phys. **13**, 1163–1167 (2017).
25. T. J. Kippenberg and K. J. Vahala, "Cavity opto-mechanics," Opt. express **15**, 17172–17205 (2007).
26. A. Schliesser, P. Del'Haye, N. Nooshi, K. Vahala, and T. J. Kippenberg, "Radiation pressure cooling of a micromechanical oscillator using dynamical backaction," Phys. Rev. Lett. **97**, 243905 (2006).
27. C. Xiong, W. H. Pernice, X. Sun, C. Schuck, K. Y. Fong, and H. X. Tang, "Aluminum nitride as a new material for chip-scale optomechanics and nonlinear optics," New J. Phys. **14**, 095014 (2012).
28. T. Carmon, H. Rokhsari, L. Yang, T. J. Kippenberg, and K. J. Vahala, "Temporal behavior of radiation-pressure-induced vibrations of an optical microcavity phonon mode," Phys. review letters **94**, 223902 (2005).
29. W. C. Jiang and Q. Lin, "Chip-scale cavity optomechanics in lithium niobate," Sci. reports **6**, 1–7 (2016).
30. L. Mercadé, L. L. Martín, A. Griol, D. Navarro-Urrios, and A. Martínez, "Microwave oscillator and frequency comb in a silicon optomechanical cavity with a full phononic bandgap," Nanophotonics **9**, 3535–3544 (2020).
31. M. Aspelmeyer, T. J. Kippenberg, and F. Marquardt, "Cavity optomechanics," Rev. Mod. Phys. **86**, 1391 (2014).
32. H. Haus, *Waves and fields in optoelectronics* (Prentice-Hall, 1984).
33. M. Poot, K. Y. Fong, M. Bagheri, W. Pernice, and H. X. Tang, "Backaction limits on self-sustained optomechanical oscillations," Phys. Rev. A **86**, 1844–1853 (2012).
34. T. F. Roque, F. Marquardt, and O. M. Yevtushenko, "Nonlinear dynamics of weakly dissipative optomechanical systems," New J. Phys. **22**, 013049 (2020).
35. M. Ludwig, B. Kubala, and F. Marquardt, "The optomechanical instability in the quantum regime," New J. Phys. **10**, 095013 (2008).
36. V. B. Braginskii and B. Manukin, Anatoliĭ, *Measurement of weak forces in physics experiments* (University of Chicago Press, 1977).
37. F. Marquardt, J. Harris, and S. M. Girvin, "Dynamical multistability induced by radiation pressure in high-finesse micromechanical optical cavities," Phys. review letters **96**, 103901 (2006).
38. L. F. Shampine and M. W. Reichelt, "The matlab ode suite," SIAM journal on scientific computing **18**, 1–22 (1997).
39. M. Bagheri, M. Poot, M. Li, W. P. Pernice, and H. X. Tang, "Dynamic manipulation of nanomechanical resonators in the high-amplitude regime and non-volatile mechanical memory operation," Nat. nanotechnology **6**, 726–732 (2011).
40. Y. Jia, J. Yan, K. Soga, and A. A. Seshia, "Parametrically excited MEMS vibration energy harvesters with design approaches to overcome the initiation threshold amplitude," J. Micromechanics Microengineering **23**, 114007 (2013).
41. Y. Jia, J. Yan, K. Soga, and A. A. Seshia, "Parametric resonance for vibration energy harvesting with design techniques to passively reduce the initiation threshold amplitude," Smart Mater. Struct. **23**, 065011 (2014).
42. M. Eichenfield, R. Camacho, J. Chan, K. J. Vahala, and O. Painter, "A picogram-and nanometre-scale photonic-crystal optomechanical cavity," nature **459**, 550–555 (2009).
43. D. Armani, T. Kippenberg, S. Spillane, and K. Vahala, "Ultra-high-q toroid microcavity on a chip," Nature **421**, 925–928 (2003).
44. M. H. Pfeiffer, J. Liu, A. S. Raja, T. Morais, B. Ghadiani, and T. J. Kippenberg, "Ultra-smooth silicon nitride waveguides based on the damascene reflow process: fabrication and loss origins," Optica **5**, 884–892 (2018).
45. Y. Tsaturyan, A. Barg, A. Simonsen, L. G. Villanueva, S. Schmid, A. Schliesser, and E. S. Polzik, "Demonstration of suppressed phonon tunneling losses in phononic bandgap shielded membrane resonators for high-q optomechanics," Opt. express **22**, 6810–6821 (2014).
46. A. H. Ghadimi, S. A. Fedorov, N. J. Engelsen, M. J. Bereyhi, R. Schilling, D. J. Wilson, and T. J. Kippenberg, "Elastic strain engineering for ultralow mechanical dissipation," Science **360**, 764–768 (2018).
47. Q. Bai, Q. Wang, D. Wang, Y. Wang, Y. Gao, H. Zhang, M. Zhang, and B. Jin, "Recent advances in brillouin optical time domain reflectometry," Sensors **19**, 1862 (2019).
48. Y. Zhang, X. Wu, Z. Ying, and X. Zhang, "Performance improvement for long-range botdr sensing system based on high extinction ratio modulator," Electron. letters **50**, 1014–1016 (2014).
49. L. Luo, B. Li, Y. Yu, X. Xu, K. Soga, and J. Yan, "Time and frequency localized pulse shape for resolution enhancement in stft-botdr," J. Sensors **2016** (2016).
50. B. Li, L. Luo, Y. Yu, K. Soga, and J. Yan, "Dynamic strain measurement using small gain stimulated brillouin scattering in stft-botdr," IEEE Sensors J. **17**, 2718–2724 (2017).